

Sapphire Nanopores for Low-Noise DNA Sensing

Pengkun Xia^{1,2,3}, Jiawei Zuo^{1,2,3}, Pravin Paudel^{1,2}, Shinhyuk Choi^{1,2,3}, Xiahui Chen^{1,2,3}, Weisi Song⁴, JongOne Im^{4,5}, Chao Wang^{1,2,3*}

¹School of Electrical, Computer and Energy Engineering, Arizona State University, Tempe, AZ, USA

²Center for Photonic Innovation, Arizona State University, Tempe, AZ, USA

³Biodesign Center for Molecular Design & Biomimetics, Arizona State University, Tempe, AZ, USA

⁴Biodesign Center for Single Molecule Biophysics, Arizona State University, Tempe, AZ, USA

⁵Current Address: INanoBio Inc., Scottsdale, AZ, USA

*E-mail: wangch@asu.edu

Abstract

Solid-state nanopores have broad applications in single-molecule biosensing and diagnostics, but their high electrical noise associated with a large device capacitance has seriously limited both their sensing accuracy and recording speed. Current strategies to mitigate the noise has focused on introducing insulating materials (such as polymer or glass) to decrease the device capacitance, but the complex process integration schemes diminish the potential to reproducibly create such nanopore devices. Here, we report a scalable and reliable approach to create nanopore membranes on sapphire with triangular shape and controlled dimensions by anisotropic wet etching a crystalline sapphire wafer, thus eliminating the noise-dominating stray capacitance that is intrinsic to conventional Si based devices. We demonstrate tunable control of the membrane dimension in a wide range from $\sim 200 \mu\text{m}$ to as small as $5 \mu\text{m}$, which corresponds to <1 pF membrane capacitance for a hypothetical 1-2 nm thick membrane. Further, we have demonstrated that a sapphire nanopore chip (~ 7 nm pore diameter in a 30 nm thick and $70 \mu\text{m}$ wide SiN membrane) has more than two-order-of-magnitude smaller device capacitance (10 pF) compared to a float-zone Si based nanopore chip (4 nm pore in 23 nm thick and $\sim 4 \mu\text{m}$ wide SiN membrane, ~ 1.3 nF), despite having a 100 times larger membrane area. The sapphire chip has a current noise of 18 pA over 100 kHz bandwidth at a 50 mV bias, much smaller than that from the Si chip (46 pA) and only slightly

29 larger than the open-headstage system noise (~11 pA). Further, we demonstrate that the sapphire
30 nanopore chip outperforms the Si chip with a higher signal-to-noise ratio (SNR, 21 versus 11),
31 despite of its thicker membrane and larger nanopore size. We believe the low-noise and high-speed
32 sensing capability of sapphire nanopore chips, together with their scalable fabrication strategy,
33 will find broad use in a number of applications in molecular sensing and beyond.

34 Introduction

35 Solid-state nanopores have attracted a lot of interest as a potentially high-speed, portable and
36 low-cost solution for detecting a variety of biomolecules, such as proteins^{1, 2, 3, 4}, RNA^{5, 6, 7} and
37 DNA^{8, 9, 10}, and studying molecular interactions^{11, 12}. However, fundamental limitations in design
38 and manufacturing of low-noise nanopore devices still remain. Currently, a major challenge in
39 prevalent silicon (Si) based solid-state nanopore sensing is associated with a large device
40 capacitance resulted from the Si conductivity. This capacitance introduces a large noise current
41 that becomes particularly dreadful at high recording frequency, thus causing serious reading errors.
42 To mitigate the noise, molecular sensing is often performed at a low bandwidth (*e.g.* 1 to 10 kHz),
43 despite the availability of low-noise, low-current amplifiers operating at much higher (100 kHz
44 and 1 MHz) bandwidth^{25, 26, 34}. Yet, demoting recording bandwidth seriously limits the signal
45 temporal resolution to ~100 microseconds, in face of the fact that the typical translocation time of
46 a single DNA base pair lies in the range 10-1,000 nanoseconds^{13, 14}. To resolve the signals with a
47 high fidelity, a number of methods have been proposed to slow down the DNA translocation speed
48 by reducing its mobility^{15, 16} or the effective external DNA-driving force^{15, 17, 18, 19}. However,
49 resorting to these methods would introduce high complexity in experiments and decrease the
50 signal-collecting throughput.

51 In fact, an alternative is to reduce the noise from the sensing system and the nanopore device
52 (more details in supplementary note 1). For instance, a recent demonstration using a customized
53 CMOS amplifier and a small-capacitance chip has demonstrated high-speed response of sub-
54 microsecond temporal resolution²⁰. Indeed, the Si chip capacitance can be as large as nano-farad
55 range if not carefully engineered (Figure S1c and Table S1). To minimize the stray capacitance,
56 conventional techniques (Table S2) introduce a thick insulating material at the nanopore vicinity

57 20, 21, 22, 23, 24, *e.g.* by selective thinning a thick membrane, dielectric coating at nanopore-
58 surrounding areas, or a combination of the two. However, many critical fabrication steps require
59 complex fabrication and manual operation, such as thick dielectric deposition, selective membrane
60 thinning, electron beam lithography, silicone/photoresist printing, glass bonding, *etc.*, and thus are
61 very expensive, slow, and difficult to reproduce. An alternative is to replace conductive silicon by
62 an insulating material, such as glass^{25, 26, 27, 28}. However, the amorphous nature of the glass
63 substrate presents complex fabrication schemes involving multiple steps of lithography, laser
64 pulling or glass etching. Even then, the process lacks precise control of the membrane
65 characteristics, causing problems in low fabrication yield, poor reproducibility, and low
66 throughput.

67 In this study, we demonstrate a manufacturable approach to create thin membranes with well-
68 controlled dimension and shape on a crystal sapphire wafer, which completely eliminates the stray
69 capacitance from conventional Si substrate. Here, we design a triangular membrane by leveraging
70 the three-fold symmetry of the sapphire lattice, and employ a batch-processing compatible
71 anisotropic sapphire wet etching process to create sapphire chips over a wafer scale. We
72 demonstrate controlled membrane dimension in a wide range from $\sim 200 \mu\text{m}$ to as small as $5 \mu\text{m}$,
73 which theoretically corresponds to pico-Farad level total chip capacitance even considering
74 nanometer-thin membranes needed in high-sensitivity DNA detection. Comparing to a float-zone
75 Si based nanopore chip, a sapphire nanopore chip with a 100 times larger membrane area still has
76 more than two-order-of-magnitude smaller device capacitance and only about one third of current
77 noise measured over 100 kHz bandwidth. Further, the sapphire nanopore outperforms the Si
78 nanopore in high-frequency detection of DNA molecules, demonstrating twice as high SNR
79 despite of having about twice as large pore diameter and 30% thicker membrane. Clearly, further

80 decreasing the membrane area and thickness and creating smaller nanopores will greatly improve
81 the detection SNR of sapphire nanopores for high-speed molecular diagnostics in a wide range of
82 applications.

83

84 **Results and discussion**

85 **Silicon oxide (SiO₂) supporting membrane formation**

86 We have devised a new strategy to create suspended dielectric membranes on sapphire by
87 anisotropic wet etching (details in Methods section). Briefly, we started with cleaning a bare 2-
88 inch c-plane (0001) sapphire wafer (Figure 1a) by RCA2 prior to depositing silicon dioxide (SiO₂)
89 by plasma-enhanced chemical vapor deposition (PECVD) on both sides (Figure 1b). SiO₂ is used
90 here for its high-selectivity in sapphire etching, experimentally determined by us as ~500:1. This
91 was followed by thermal annealing to release the SiO₂ stress, which otherwise would result in film
92 crack during high-temperature sapphire etching (Figure S2). Then we patterned one side (cavity
93 side) of the SiO₂ by photolithography and reactive-ion etching (RIE) into a triangular shaped mask
94 layer (Figure 1c). Subsequently, hot sulfuric acid and phosphoric acid were used to etch through
95 the sapphire wafer to suspend the SiO₂ membrane as a supporting layer (Figure 1d).

96 Considering the three-fold symmetric crystal structure of c-plane sapphire wafer, we designed
97 the SiO₂ etching window as a triangle to control the membrane shape and dimension. The sapphire
98 facet evolution is highly dependent on the alignment of the etching mask to the sapphire crystal,
99 similar to anisotropic Si etching, but more complex given its hexagonal lattice nature^{29, 30}. We
100 studied the geometry evolution of the SiO₂ membrane by rotating the SiO₂ membrane relative to
101 the sapphire crystal (Figure S3). In another word, we kept the triangular mask dimension the same
102 but changed its alignment angle to the sapphire flat (A-plane), denoted as window-to-flat angle α ,

103 and indeed found intriguing formation of membranes. For example, two different sets of triangular
104 membranes were formed when $0 < \alpha < 20^\circ$ and $40^\circ < \alpha < 60^\circ$, with a rotational angle offset
105 between the two at $\sim 30^\circ$. In contrast, complex polygon membranes with up to nine sides emerged
106 when $20^\circ < \alpha < 40^\circ$, where six of the sides were parallel to the sides of the above-mentioned two
107 triangular membranes. Additionally, the membrane area was also found sensitive to α , yielding an
108 area of more than three orders of magnitude larger when $\alpha \sim 30^\circ$ compared to $\alpha \sim 0^\circ$. Here we
109 believe the facet evolution is related to the etching rate differences between different sapphire
110 crystal planes. Given that the M- and A- planes have very slow etching rates and are perpendicular
111 to the c-plane, they are believed to be less relevant in the observed cavity formation. We suspect
112 that the R- and N-planes of the sapphire crystals are most relevant³¹, and their competition could
113 result in the angle-dependent evolution into membranes in triangles or nonagon. Drastically
114 different from the triangular design, square window design produced irregular and complex
115 membranes that are much more difficult to control (Figure S4).

116 Here we chose a designed alignment angle of $\alpha \sim 0^\circ$ and we performed theoretical calculation
117 to estimate the relationship between the membrane and the mask dimensions (details in
118 supplementary note 2), and determined that the membrane triangle length L_2 could be simply
119 engineered by the mask triangle length L_1 following $L_1 = L_2 + 2\sqrt{3}h / \tan \theta$ (Figure 2a), where
120 h is the sapphire wafer thickness and θ is an effective angle between the exposed facets in the
121 cavity and sapphire c-plane that can be empirically determined.

122 We also intentionally included rectangular dicing marks surrounding the cavity etching
123 windows during lithography, creating trenches in sapphire after acid etching that allowed us to
124 hand-dice sapphire into 5 mm by 5 mm square chips (Figure 2c), which would otherwise be very
125 challenging given the hexagonal lattice of sapphire. This 5 mm chip size was designed to fit into

126 our fluidic jig and transmission electron microscopy (TEM) holder for nanopore drilling and
127 electrical characterization. The final obtained SiO₂ membrane on sapphire was 3 μm thick, and
128 intact during the etching and chip dicing process (Figure 2d-e). The SiO₂ thickness was only
129 reduced slightly from the original 3.5 μm while masking the etching of 250 μm sapphire, indicating
130 an ultra-high etching selectivity of ~500:1. The SiO₂ membrane size L_2 was also found tunable in
131 a wide range from 5 to 200 μm (Figure 2f-g, more images in Figure S5a). The 5 μm membrane
132 corresponds to a theoretical pico-farad chip capacitance even for nanometer-thin membranes (*e.g.*
133 ~0.3 pF membrane capacitance for a hypothetical 2 nm thick SiN membrane (dielectric constant
134 = 6.5), ~0.2 pF sapphire cavity capacitance and ~1.4 pF sapphire substrate capacitance within the
135 o-ring area. Details in Table S3), which are highly desired for high-SNR^{6, 32} DNA detection. We
136 further fitted the correlation between L_1 and L_2 using our theoretical model, and determined an
137 effective facet angle $\theta \sim 50^\circ$ (Figure S5d). This experiment proved that it was possible to control
138 and create ultrasmall membranes for functional sapphire chips. It was also intriguing to notice the
139 complex sapphire facets from scanning-electron microscope (SEM) image of the formed cavity
140 (Figure S6a), attributed to the complex crystal structure of sapphire and particularly possibly due
141 to the competition between R- and N-planes of the sapphire crystals.

142

143 **SiN thin membrane formation**

144 Using the triangular SiO₂ membranes formed by sapphire etching, we have developed a process
145 to create thin SiN membranes suitable for nanopore formation and DNA sensing⁶. Briefly, we
146 deposited low-stress SiN film on the suspended SiO₂ membranes by low-pressure chemical vapor
147 deposition (LPCVD), and then removed the SiO₂ film within the triangular aperture via selective
148 dry etching and HF based wet etching from the cavity side (Figure 1f). Using the SiN film instead

149 of the remaining SiO₂ mask layer as the membrane material allows us to precisely control the
150 membrane thickness, and largely eliminates high compressive stress from the SiO₂ layer that
151 negatively affects the membrane integrity. To thin down the SiN membrane to desired thickness,
152 we evaluated both reactive ion etching (RIE) and hot phosphoric acid based wet etching. We found
153 that RIE could cause non-uniformity (Figure S7a) and might damage the membrane, causing
154 current leakage, as shown by current-voltage (IV) characteristics using one molar potassium
155 chloride solution (1M KCl) (Figure S7b). In contrast, hot phosphoric acid wet etching yielded
156 uniform SiN membrane (Figure S7c and Figure S8b) without current leakage (Figure S7d), thus
157 preferable for the DNA sensing test. Finally, a nanopore was drilled on the SiN membrane on the
158 sapphire chip (Figure 3 a-b) and a float-zone Si chip (SiMPore Inc., Figure S9), the best high-
159 resistivity chips available to us as a reference, by TEM (Figure 1g) for electrical characterization
160 and DNA sensing test.

161

162 **Noise characterization**

163 First we experimentally characterized the device capacitance of the sapphire and Si nanopore
164 chips. Noticeably, the sapphire chip had a 100 times larger membrane area (68 μm triangular side
165 length, or $\sim 2000 \mu\text{m}^2$) than the Si chip ($4.2 \times 4.7 \mu\text{m}$ square, or $\sim 20 \mu\text{m}^2$) and slightly thicker SiN
166 (30 nm for sapphire and 23 nm for Si). Following $C_m = \epsilon_r \epsilon_0 \frac{A}{d}$, where C_m is the membrane
167 capacitance, ϵ_r is the relative permittivity of SiN, ϵ_0 is the vacuum permittivity, A is the
168 membrane area and d is the membrane thickness, we calculated the sapphire membrane
169 capacitance as 3.8 pF, more than 70 times bigger than that of the Si chips (0.05 pF). However, the
170 sapphire chip was experimentally found to have a much smaller total capacitance (~ 10 pF)
171 compared to the Si chip (1.34 nF) using the Clampex software (Molecular Devices, LLC). This

172 clearly demonstrated that the use of insulating sapphire successfully eliminated the dominant
173 capacitance resulted from substrate conductivity, thus appealing to low-noise measurement.

174 We further analyzed the ionic current noise for the sapphire nanopore, the Si nanopore and the
175 open-headstage system (Axopatch 200B) under 10 kHz and 100 kHz low-pass filter (Figure 3c).
176 The root-mean-square (RMS) of the measured current of the sapphire nanopore chip is ~5 and 18
177 pA using 10 and 100 kHz filters, only slightly higher than the open-stage values of 3 and 11 pA
178 but much better than those from Si nanopore (~16 and 46 pA). Additionally, the power spectral
179 density (PSD) of Si and sapphire nanopores (Figure 3d) demonstrated that the noise power of
180 sapphire nanopore was about one order larger than the Si nanopore for a wide range of bandwidth,
181 consistent with its low-current-noise performance. The noise power of the sapphire nanopore at
182 low frequency range (<100 Hz) was slightly higher than Si, which could result from the flicker
183 noise and the large dielectric noise due to the large membrane size in the sapphire nanopore³³.
184 Comparing with the existing noise-mitigating techniques^{22, 24, 27, 28, 34, 35} (Table S2), our sapphire
185 nanopore requires no additional or manual fabrication steps to reduce the device capacitance. This
186 batch-processing-compatible design and fabrication strategy makes sapphire an excellent
187 candidate for low-noise and high-frequency nanopore sensing at a low cost.

188

189 **DNA detection**

190 To evaluate the performance in the detection of DNA molecules by our sapphire nanopore,
191 1kbp ds-DNA translocation events were measured under 100 kHz (Figure 4) and 10 kHz (Figure
192 S10) low-pass filter for both the sapphire and the Si nanopore under 50 mV, 100 mV and 150 mV
193 bias. Comparing representative ionic current traces of 1kbp dsDNA (Figure 4b) for both Si and
194 sapphire nanopores, we note that the DNA signals collected by Si nanopore were more irregular,

195 particularly at lower bias voltages. These irregular signals, together with the high baseline noise,
196 made it very challenging to faithfully distinguish DNA signals from the background. In
197 comparison, the sapphire nanopore produced much cleaner DNA signals at 100 kHz bandwidth
198 that can be easily separated from the noise. Additionally, we also show that recording at lower
199 frequencies (such as 10 kHz) would result in serious data loss of the fast DNA signals, thus
200 presenting only longer and in some occasions distorted signals^{34, 36}. Clearly, sapphire nanopores
201 enable preferable high-speed, high-throughput, and high-fidelity detection of DNA signals.

202 To study the DNA translocation mechanism, we extracted the DNA signals by OpenNanopore
203 Program³⁷. We scatter-plotted the fractional blockade current $I_B (=i_b/i_o)$ and the dwelling time Δt
204 of all the DNA events from the sapphire chip under 50 mV (Figure 4c). Here i_b is the blocked-pore
205 current and i_o is the open pore current. The use of I_B allowed us to eliminate the impact of bias
206 difference on DNA signal analysis. Two distinct populations were observed (separated by the red
207 dashed line in Figure 4d) and recognized as the translocation events (green oval) and the collision
208 events (pink oval)¹¹. Further, we analyzed the current blockade distribution and fitted with
209 Gaussian function (Figure 4d), producing two distinct I_B populations attributed to translocation
210 and collisions. We further analyzed the dwelling time Δt of each of the two event populations and
211 fitted with exponential decay function (black lines, Figure 4e). It showed that the translocation
212 events (green, top panel) had a longer tail (decay constant=16.19 μs) than the collision events
213 (decay constant=8.45 μs), consistent with previous studies¹¹.

214 We further applied this signal segregation approach to analyze all the DNA signals collected
215 from the Si and sapphire nanopores (Figure 5 a-d). By scatter-plotting the normalized DNA
216 blockade signal ($1-I_B =\Delta I/i_o$) and marking the current noise (I_{RMS} , dash-dot lines) at each bias
217 voltage (black: 50 mV, red: 100 mV, blue: 150 mV, Figure 5e-f), we could investigate the SNR

218 (defined here as $\frac{1-I_B}{I_{RMS}}$) of the true DNA translation signals. The short solid lines represented the
219 average DNA signals ($1-I_B$) determined from the Gaussian distribution of the translocation events
220 (Figure 5b, d). The sapphire nanopores produced slightly smaller DNA signal amplitude than Si
221 nanopores, because of their larger pore size and thicker membrane. However, given the suppressed
222 noise current, the sapphire nanopore still evidently outperformed Si nanopore in SNR. For example,
223 the sapphire nanopore had a SNR of 21 at 150 mV bias, almost twice as good as the Si nanopore.

224 We further attempted to detect short single-stranded (ss) DNA molecules using sapphire
225 nanopores (Figure 6). Here ionic current traces of Poly(A)₄₀ ssDNA translocation events were
226 recorded under 100 kHz low-pass filter with the voltages from 100 mV to 150 mV. We performed
227 the same analysis to investigate the SNR of this ssDNA (Figure 6b and Figure S11), and obtained
228 a SNR of ~6 for both 100 mV and 150 mV bias voltages. This provided evidence that the sapphire
229 nanopores can detect a wide range of biomolecules of different sizes. We expect the SNR can be
230 remarkably enhanced by using thinner membrane thickness and small nanopore in future studies.

231

232 **Conclusion**

233 In conclusion, we demonstrate a novel design and manufacturable approach to create sapphire
234 nanopores featuring triangular membranes with well-controlled dimensions and shapes.
235 Completely eliminating the stray capacitance, the sapphire nanopores convincingly produced two-
236 order-of-magnitude smaller device capacitance compared to a float-zone Si based nanopore (10
237 pF versus ~1.3 nF) despite having a 100 times larger membrane area. Accordingly, the sapphire
238 nanopores generated ~5 times smaller RMS ionic current noise than a Si nanopore at 100 kHz
239 bandwidth, and resulted in high-fidelity DNA sensing with a twice higher SNR while having a
240 larger nanopore size and thicker SiN membrane. This novel sapphire nanopore sensor architecture

241 will enable a new way of high-volume and cost-effective manufacturing of low-noise solid-state
242 nanopores for detecting a wide range of biomolecules and studying the fundamental biophysics
243 and molecule-molecule interactions at single-molecule level.

244 **Methods**

245 (1) Sapphire nanopore membrane fabrication

246 Firstly, a 250 μm thick 2-inch c-plane sapphire wafer (Precision Micro-Optics Inc.) was treated by
247 RCA2 cleaning (deionized water: 27% hydrochloric acid: 30% hydroperoxide = 6: 1: 1, 70 °C) for
248 15 min followed by 3.5 μm PECVD SiO_2 deposition (Oxford PECVD, 350 °C, 20 W, 1000 mTorr,
249 SiH_4 170 sccm, N_2O 710 sccm, deposition rate: 68 nm/min) on both sides. Then the wafer was
250 brought in a furnace for thermal annealing (400 °C, 2 hrs, air ambient) to release the stress in SiO_2
251 film, followed by photolithography (Heidelberg Instruments μPG 101 laser writer, 600 nm AZ
252 1505 photoresist) and RIE (PlasmaTherm 790 RIE Fluorine, 250 W bias, 40 mTorr, CHF_3 40 sccm,
253 O_2 3 sccm, etching rate: 46 nm/min) etching on SiO_2 to form a triangular etching window. Next,
254 hot sulfuric acid and phosphoric acid (3:1, hot plate 540 °C) were used to etch through the sapphire
255 wafer (etching rate: 12 $\mu\text{m/hr}$) and suspend the SiO_2 membrane. To ensure the safety of handling
256 hot and concentrated acids, we custom-designed a quartz glassware setup suitable for high-
257 temperature acid-based sapphire etching process. We intentionally placed the sapphire wafer
258 vertically in a 2-inch glass boat in the etching container to minimize possible damage to the
259 membrane by the boiling acids (Figure S12). After the acid was added into the quartz glassware,
260 we loaded the 2-inch glass boat with the wafer into the quartz glassware, and installed a clamp seal
261 and a condenser column to minimize acid vapor leakage. Finally we raised up the temperature of
262 the hot plate to 540 °C (100-200 °C/min) to start the etching. Following that, the SiO_2 membrane
263 was thinned down by RIE (PlasmaTherm 790 RIE Fluorine, 250 W bias, 40 mTorr, CHF_3 40 sccm,
264 O_2 3 sccm, etching rate: 46 nm/min) to 1.45 μm , and a layer of SiN (320 nm) was deposited onto
265 the SiO_2 membrane by LPCVD (Tystar TYTAN 4600, 250 mTorr, DCS flow 25 sccm, NH_3 flow
266 75 sccm, 750 °C, deposition rate: 6 nm/min). SiN unintentionally deposited in the back cavity of

267 the chip was removed by a RIE etching step (PlasmaLab 80 Fluorine, 100 W bias, 100 mTorr, CF₄
268 50 sccm, O₂ 2 sccm, etching rate: 61 nm/min). Then hydrofluoric acid (8%) was used to remove
269 the SiO₂ layer to suspend the SiN layer (90 nm/min). The final SiN membrane was thinned down
270 by hot 85% phosphoric acid (hot plate 245 °C, etching rate: ~25 nm/min) to desired thickness.

271

272 (2) Si nanopore membrane fabrication

273 The Si nanopore membranes were purchased from SiMPore Inc. A 100 mm diameter 200 μm thick
274 float-zone Si wafer with ~100 nm thermal SiO₂ and ~20 nm LPCVD SiN was etched by alkali to
275 create a Si cavity array. Then the thermal SiO₂ was removed to produce an array of 4-5 μm
276 suspended SiN membranes. Then SiO₂ and SiN film thicknesses were confirmed by M-2000
277 ellipsometer (J.A. Woollam Co.) as 99nm and 23nm by us.

278

279 (3) Thickness characterization on the small membranes

280 The thicknesses of membranes were measured by Filmetrics F40 (Filmetrics Inc.), which has the
281 capability to measure small area and is based on the reflectance and the refractive index of the
282 measured material. For the LPCVD SiN membranes, the refractive index was first fitted using the
283 same-batch LPCVD SiN deposited on Si by Woollam Spectroscopic Ellipsometer (J.A. Woollam
284 Co.). Then the refractive index list was exported to Filmetrics F40 to measure the thickness of the
285 SiN suspended membrane (film stack: air-SiN-air). A well-fitting curve of the central region of the
286 triangular membrane was shown in Figure S8a.

287

288 (4) Nanopore drilling

289 The nanopore was drilled by JEOL 2010F TEM. The 5 mm by 5 mm nanopore chip was placed in
290 a customized 5 mm TEM sample holder. The largest condenser aperture and spot size 1 were used
291 for maximum beam current output. After the alignment was finished, the imaging magnification
292 was increased to 1.5M (maximum). The beam spot was spread to 3 inch and held for 5-15 min for
293 stabilization. If the beam spot drifted, the focus needed to be re-adjusted under 250K magnification
294 and the stabilization needed to be re-monitored under 1.5M magnification. Once the beam got
295 stabilized, the 3-inch beam spot was reduced to ~7 mm and the condenser astigmatism was quickly
296 adjusted to make the spot as round as possible. At this stage, from the eyepiece, the material being
297 bombarded could be observed. Once it was clear, a successful drilling was identified. Under the
298 condition of 7 kV A2 and 30 nm membrane, it took 75-90 sec to drill through the membrane.

299

300 (5) Noise characterization, DNA preparation and DNA sensing

301 The TEM-drilled nanopore chip was treated with UV ozone cleaner (ProCleanerTM, BioForce
302 Nanosciences Inc.) for 15 min to improve the hydrophilicity of the surface and mounted into a
303 customized flow cell (Figure S13). Then a solution of 1:1 mixed ethanol and DI water was injected
304 into the flow cell to wet the chip for 30 min. The solution was subsequently flushed away by
305 injection of DI water. Next, 100 millimolar (mM) KCl was injected into the flow cell to test the
306 current-voltage (IV) curve using Axopatch 200B amplifier and Digidata 1440A digitizer
307 (Molecular Devices, LLC.), and then 1M KCl solution was injected to characterize the device
308 current. To do DNA sensing, the 1kbp as-ordered dsDNA (Thermo Scientific NoLimits, Thermo
309 Fisher Scientific Inc.) was diluted using 1M KCl to 5 ng/ μ L or the Poly(A)₄₀ ssDNA (Standard
310 DNA oligonucleotides, Thermo Fisher Scientific Inc.) was diluted using 1M KCl to 50nM, and
311 stirred using a vortex mixer. Finally, the DNA solution was injected into the flow cell to collect

312 DNA signals under 10 kHz and 100 kHz low-pass filter at 50, 100 and 150 mV using Axopatch
313 200B amplifier and Digidata 1440A digitizer (Molecular Devices, LLC.). The flow cell was kept
314 in a customized Faraday cage on an anti-vibration table (Nexus Breadboard, Thor labs) to isolate
315 the environment noise during measurement.

316

317 (6) DNA signal collection and analysis

318 After the injection of the DNA solution, once the external voltage was applied, DNA signal could
319 be observed from the Clampex software. The DNA signals were recorded for sufficient time at
320 each voltage (50, 100, 150 mV) and each frequency (10 and 100 kHz) to ensure a relatively large
321 data set for analysis. The collected DNA signals were analyzed by OpenNanopore program ³⁷.
322 Firstly we edited a MATLAB program to convert all the .abf files to .mat files in a batch. Then
323 these .mat files were imported to OpenNanopore program to generate the dwelling time and
324 blockade current amplitude data of each DNA signal for subsequent analysis.

325 **Acknowledgments**

326 This work is partially supported by the Arizona State University (ASU) startup funds to Prof.
327 Chao Wang and National Science Foundation under award no. 1711412, 1809997, 1838443 and
328 1847324. We thank Prof. Amit Meller at Technion - Israel Institute of Technology, Dr. Yann
329 Astier and Dr. Juraj Topolancik from Roche Sequencing Solutions, Dr. Stuart Lindsay at ASU,
330 and Dr. Pei Pang (currently with Roswell Biotechnologies) at ASU for fruitful discussions.

331 **References**

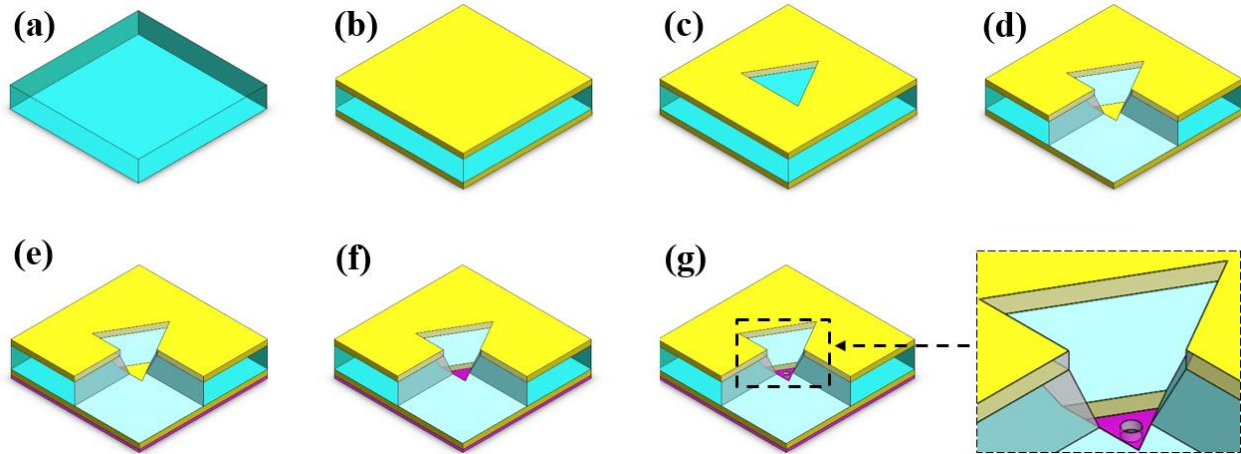
- 332 1. Varongchayakul N, Song J, Meller A, Grinstaff MW. Single-molecule protein sensing in
333 a nanopore: a tutorial. *Chemical Society Reviews* 2018, **47**(23): 8512-8524.
- 334 2. Li W, Bell NA, Hernández-Ainsa S, Thacker VV, Thackray AM, Bujdoso R, *et al.* Single
335 protein molecule detection by glass nanopores. *ACS nano* 2013, **7**(5): 4129-4134.
- 336 3. Wang C, Fu Q, Wang X, Kong D, Sheng Q, Wang Y, *et al.* Atomic layer deposition
337 modified track-etched conical nanochannels for protein sensing. *Analytical chemistry*
338 2015, **87**(16): 8227-8233.
- 339 4. Yusko EC, Bruhn BR, Eggenberger OM, Houghtaling J, Rollings RC, Walsh NC, *et al.*
340 Real-time shape approximation and fingerprinting of single proteins using a nanopore.
341 *Nature nanotechnology* 2017, **12**(4): 360.
- 342 5. Shasha C, Henley RY, Stoloff DH, Rynearson KD, Hermann T, Wanunu M. Nanopore-
343 based conformational analysis of a viral RNA drug target. *ACS nano* 2014, **8**(6): 6425-
344 6430.
- 345 6. Wanunu M, Dadosh T, Ray V, Jin J, McReynolds L, Drndić M. Rapid electronic
346 detection of probe-specific microRNAs using thin nanopore sensors. *Nat Nanotechnol*
347 2010, **5**(11): 807-814.
- 348 7. Henley RY, Carson S, Wanunu M. Studies of RNA sequence and structure using
349 nanopores. *Progress in molecular biology and translational science*, vol. 139. Elsevier,
350 2016, pp 73-99.
- 351 8. Dekker C. Solid-state nanopores. *Nature nanotechnology* 2007, **2**(4): 209.
- 352 9. Wanunu M. Nanopores: A journey towards DNA sequencing. *Physics of life reviews*
353 2012, **9**(2): 125-158.

- 354 10. Shi W, Friedman AK, Baker LA. Nanopore sensing. *Analytical chemistry* 2016, **89**(1):
355 157-188.
- 356 11. Wanunu M, Sutin J, McNally B, Chow A, Meller A. DNA translocation governed by
357 interactions with solid-state nanopores. *Biophysical journal* 2008, **95**(10): 4716-4725.
- 358 12. Kwak DK, Chae H, Lee MK, Ha JH, Goyal G, Kim MJ, *et al.* Probing the small-
359 molecule inhibition of an anticancer therapeutic protein-protein interaction using a solid-
360 state nanopore. *Angewandte Chemie* 2016, **128**(19): 5807-5811.
- 361 13. Feng J, Liu K, Bulushev RD, Khlybov S, Dumcenco D, Kis A, *et al.* Identification of
362 single nucleotides in MoS₂ nanopores. *Nature nanotechnology* 2015, **10**(12): 1070.
- 363 14. Schneider GF, Kowalczyk SW, Calado VE, Pandraud G, Zandbergen HW, Vandersypen
364 LM, *et al.* DNA translocation through graphene nanopores. *Nano letters* 2010, **10**(8):
365 3163-3167.
- 366 15. Fologea D, Uplinger J, Thomas B, McNabb DS, Li J. Slowing DNA translocation in a
367 solid-state nanopore. *Nano letters* 2005, **5**(9): 1734-1737.
- 368 16. Zhang Y, Wu G, Ma J, Yuan Z, Si W, Liu L, *et al.* Temperature effect on translocation
369 speed and capture rate of nanopore-based DNA detection. *Science China Technological*
370 *Sciences* 2015, **58**(3): 519-525.
- 371 17. Keyser UF, Koeleman BN, Van Dorp S, Krapf D, Smeets RM, Lemay SG, *et al.* Direct
372 force measurements on DNA in a solid-state nanopore. *Nature Physics* 2006, **2**(7): 473.
373
- 374 18. Trepagnier EH, Radenovic A, Sivak D, Geissler P, Liphardt J. Controlling DNA capture
375 and propagation through artificial nanopores. *Nano letters* 2007, **7**(9): 2824-2830.

- 376 19. He Y, Tsutsui M, Fan C, Taniguchi M, Kawai T. Controlling DNA translocation through
377 gate modulation of nanopore wall surface charges. *ACS nano* 2011, **5**(7): 5509-5518.
- 378 20. Shekar S, Niedzwiecki DJ, Chien C-C, Ong P, Fleischer DA, Lin J, *et al.* Measurement of
379 DNA translocation dynamics in a solid-state nanopore at 100 ns temporal resolution.
380 *Nano letters* 2016, **16**(7): 4483-4489.
- 381 21. Dimitrov V, Mirsaidov U, Wang D, Sorsch T, Mansfield W, Miner J, *et al.* Nanopores in
382 solid-state membranes engineered for single molecule detection. *Nanotechnology* 2010,
383 **21**(6): 065502.
- 384 22. Rosenstein JK, Wanunu M, Merchant CA, Drndic M, Shepard KL. Integrated nanopore
385 sensing platform with sub-microsecond temporal resolution. *Nature methods* 2012, **9**(5):
386 487.
- 387 23. Venta K, Shemer G, Puster M, Rodriguez-Manzo JA, Balan A, Rosenstein JK, *et al.*
388 Differentiation of short, single-stranded DNA homopolymers in solid-state nanopores.
389 *ACS nano* 2013, **7**(5): 4629-4636.
- 390 24. Balan A, Machielse B, Niedzwiecki D, Lin J, Ong P, Engelke R, *et al.* Improving signal-
391 to-noise performance for DNA translocation in solid-state nanopores at MHz bandwidths.
392 *Nano letters* 2014, **14**(12): 7215-7220.
- 393 25. Steinbock LJ, Bulushev RD, Krishnan S, Raillon C, Radenovic A. DNA translocation
394 through low-noise glass nanopores. *Acs Nano* 2013, **7**(12): 11255-11262.
- 395 26. Pitchford WH, Kim H-J, Ivanov AP, Kim H-M, Yu J-S, Leatherbarrow RJ, *et al.*
396 Synchronized optical and electronic detection of biomolecules using a low noise
397 nanopore platform. *ACS nano* 2015, **9**(2): 1740-1748.

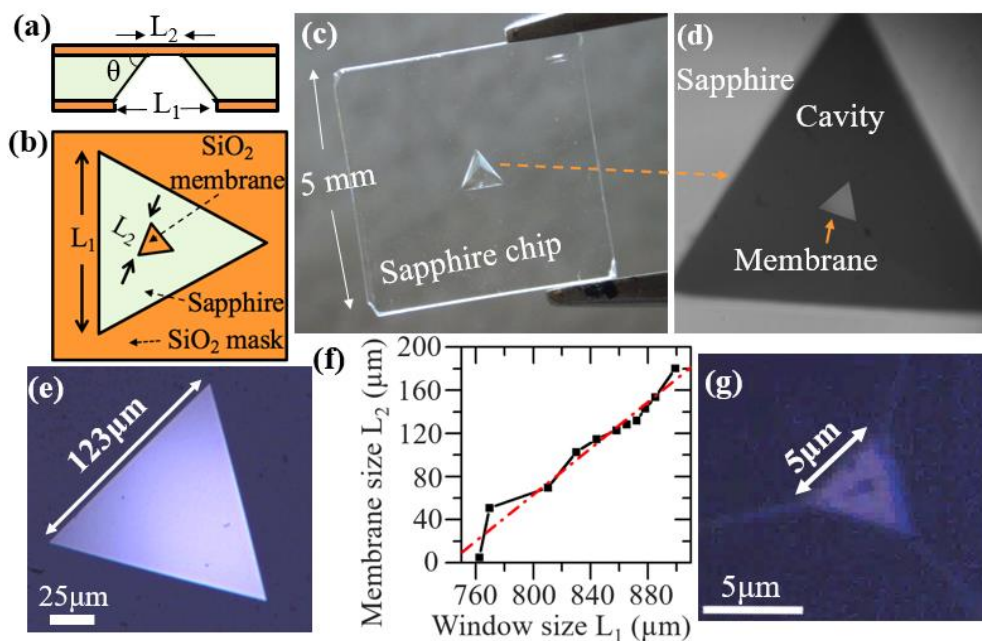
- 398 27. Lee M-H, Kumar A, Park K-B, Cho S-Y, Kim H-M, Lim M-C, *et al.* A low-noise solid-
399 state nanopore platform based on a highly insulating substrate. *Scientific reports* 2014, **4**:
400 7448.
- 401 28. Balan A, Chien C-C, Engelke R, Drndić M. Suspended solid-state membranes on glass
402 chips with sub 1-pf capacitance for biomolecule sensing applications. *Scientific reports*
403 2015, **5**: 17775.
- 404 29. Chen Y-C, Hsiao F-C, Lin B-W, Wang B-M, Wu YS, Hsu W-C. The formation and the
405 plane indices of etched facets of wet etching patterned sapphire substrate. *Journal of The*
406 *Electrochemical Society* 2012, **159**(6): D362-D366.
- 407 30. Chen C-C, Hsiao FC, Lin B-W, Hsu W-C, Wu YS. Evolution of bottom c-Plane on wet-
408 etched patterned sapphire substrate. *ECS Journal of Solid State Science and Technology*
409 2013, **2**(9): R169-R171.
- 410 31. Xing Y, Guo Z, Gosálvez MA, Wu G, Qiu X. Characterization of anisotropic wet etching
411 of single-crystal sapphire. *Sensors and Actuators A: Physical* 2019: 111667.
- 412 32. Rodriguez-Manzo JA, Puster M, Nicolai A, Meunier V, Drndic M. DNA translocation in
413 nanometer thick silicon nanopores. *ACS nano* 2015, **9**(6): 6555-6564.
- 414 33. Wen C, Zeng S, Arstila K, Sajavaara T, Zhu Y, Zhang Z, *et al.* Generalized noise study
415 of solid-state nanopores at low frequencies. *ACS sensors* 2017, **2**(2): 300-307.
- 416 34. Park K-B, Kim H-J, Kim H-M, Han SA, Lee KH, Kim S-W, *et al.* Noise and sensitivity
417 characteristics of solid-state nanopores with a boron nitride 2-D membrane on a pyrex
418 substrate. *Nanoscale* 2016, **8**(10): 5755-5763.

- 419 35. Wanunu M, Dadosh T, Ray V, Jin J, McReynolds L, Drndić M. Rapid electronic
420 detection of probe-specific microRNAs using thin nanopore sensors. *Nature*
421 *nanotechnology* 2010, **5**(11): 807.
- 422 36. Rosenstein JK, Wanunu M, Merchant CA, Drndic M, Shepard KL. Integrated nanopore
423 sensing platform with sub-microsecond temporal resolution. *Nat Methods* 2012, **9**(5):
424 487-492.
- 425 37. Raillon C, Granjon P, Graf M, Steinbock LJ, Radenovic A. Fast and automatic processing
426 of multi-level events in nanopore translocation experiments. *Nanoscale* 2012, **4**(16):
427 4916-4924.

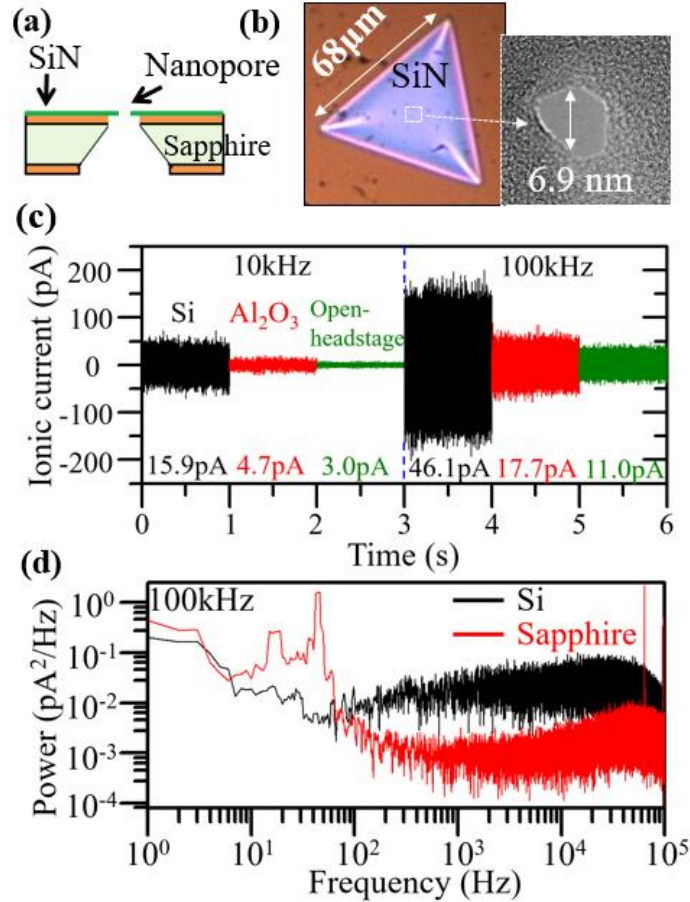


428

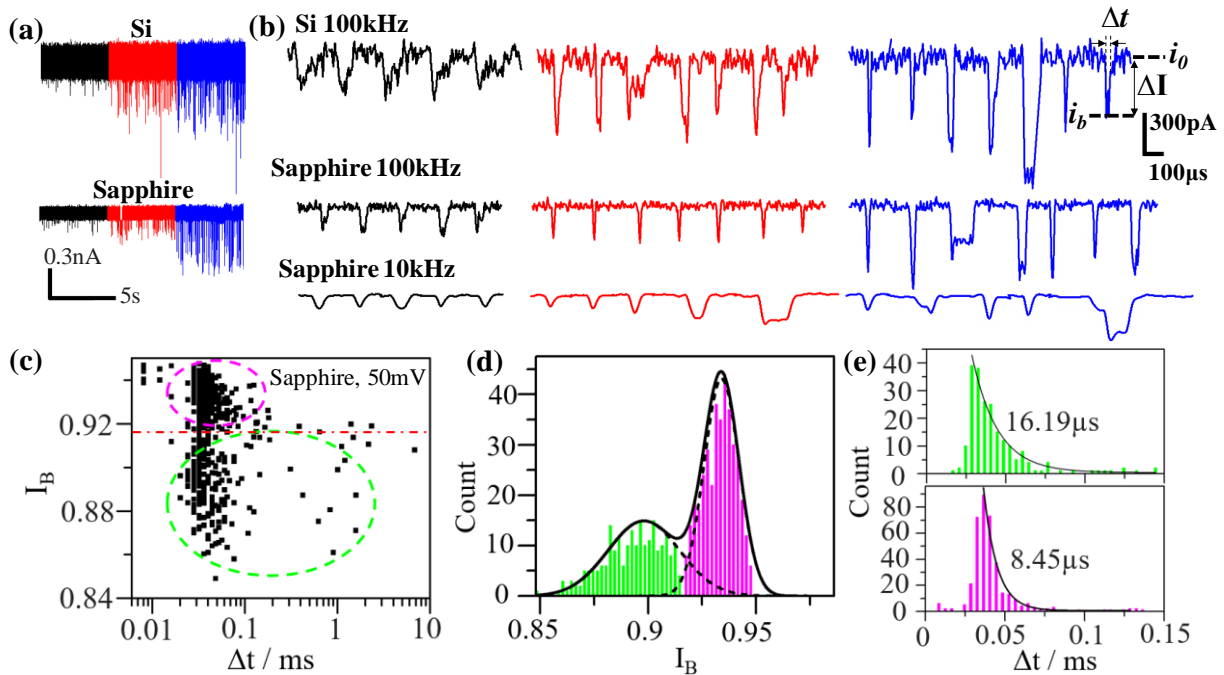
429 Figure 1. Schematics showing the key steps for creating the membrane and the nanopore on a
430 sapphire substrate. (a) A 250 μm sapphire wafer is cleaned by solvents and RCA2. (b) A layer of
431 PECVD SiO_2 is deposited on both sides of the sapphire wafer, followed by thermal annealing. (c)
432 A window is formed in the top SiO_2 by photolithography and RIE. (d) The sapphire is etched
433 through in hot sulfuric acid and phosphoric acid, forming the suspended SiO_2 membrane at the
434 bottom. (e) A thin layer of LPCVD SiN is deposited on the bottom SiO_2 membrane, and the
435 unintentionally deposited SiN in the cavity is etched by RIE to expose the SiO_2 membrane in the
436 cavity (not shown). (f) The thin SiN membrane is formed by firstly selectively removing the SiO_2
437 membrane in the cavity using hydrofluoric acid and then thinning the SiN using hot phosphoric
438 acid. (g) A nanopore is drilled by transmission electron microscope (TEM) on the SiN membrane.
439 One corner of the chip was hidden in schematic d-g to better show the central etching cavity.



440
441 Figure 2. The formation of the SiO_2 supporting membrane after sapphire etching. (a) Side-view
442 schematic of the chip. L_1 and L_2 are the window size and the membrane size respectively. θ is the
443 effective facet angle after etching. (b) Top-view schematic of the chip. (c) An optical image of a 5
444 mm by 5 mm sapphire chip with intact SiO_2 membrane. (d) Optical image showing both the
445 triangular window and the SiO_2 membrane. (e) Optical image of a representative triangular SiO_2
446 membrane ($123\ \mu\text{m}$ side length). (f) Quasi-linear relation between the membrane size (L_2) and the
447 window size (L_1). (g) Optical image of a representative small SiO_2 membrane ($5\ \mu\text{m}$).



448
449 Figure 3. Ionic current noise analysis of the sapphire nanopore and the Si nanopore chips. (a) A
450 schematic of the measured sapphire nanopore chip. (b) An optical image of the SiN membrane of
451 the sapphire nanopore chip and a TEM image of the drilled nanopore. (c) The ionic current noise
452 for the Si nanopore (black traces), the sapphire nanopore (red traces), and the open-headstage state
453 (green traces) under 10 kHz (left three traces) and 100 kHz (right traces) low-pass filter
454 respectively. The two chips were both measured under 50 mV voltage. The RMS ionic current
455 values are given for each measurement. (d) Power spectra of the current noise of the sapphire
456 nanopore and the Si nanopore versus frequency under 100 kHz low-pass filter. The two chips were
457 both measured under 50 mV voltage.



458

459 Figure 4. Analysis of 1kbp dsDNA translocation events for the sapphire nanopore ($2002 \mu\text{m}^2$

460 membrane area) and the Si nanopore ($31 \mu\text{m}^2$ membrane area) under 100 kHz filter frequency. (a)

461 The current traces of the DNA translocation events of the Si nanopore and the sapphire nanopore

462 under different voltages (black: 50 mV, red: 100 mV, blue: 150 mV). (b) Representative DNA

463 events for the Si nanopore and the sapphire nanopore at different voltages (black: 50 mV, red: 100

464 mV, blue: 150 mV) and different recording bandwidth (top two rows: 100 kHz, bottom row: 10

465 kHz). Δt : event dwelling time; i_0 : open-pore current baseline; i_b : block-pore current level; ΔI :

466 blockade current amplitude. (c) Scatter plot of the fractional blockade current $I_B (=i_b/i_0)$ versus the

467 dwelling time Δt of all the DNA events from the sapphire nanopore under 50 mV. Two distinct

468 populations are separated by the red dashed line as the translocation events (green oval) and the

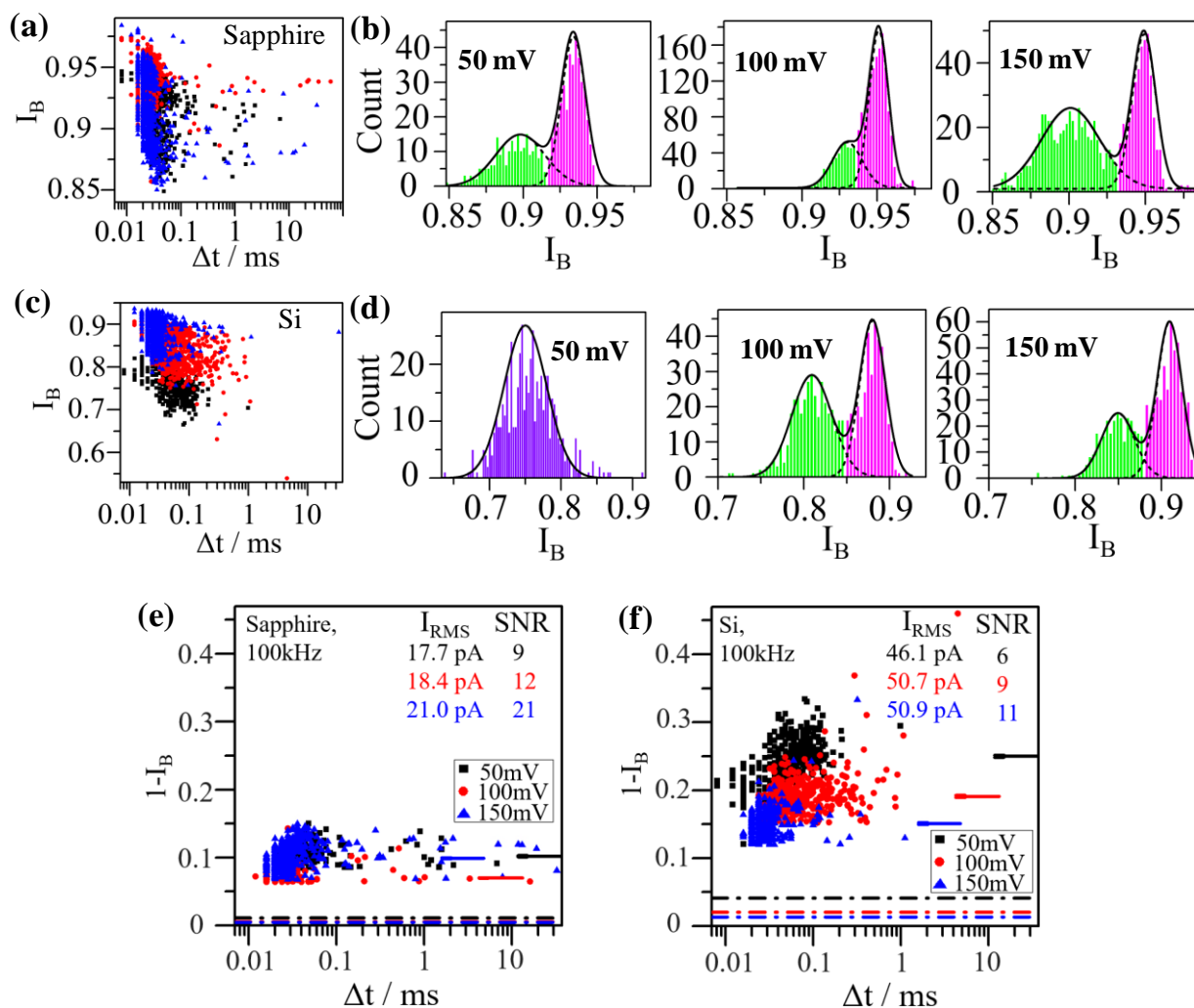
469 collision events (pink oval). (d) The histograms of I_B of the sapphire nanopore under 50 mV

470 displaying two distinct peaks corresponding to the translocation events (green bars) and the

471 collision events (pink bars). The solid and dash black lines indicate the fitting by Gaussian function.

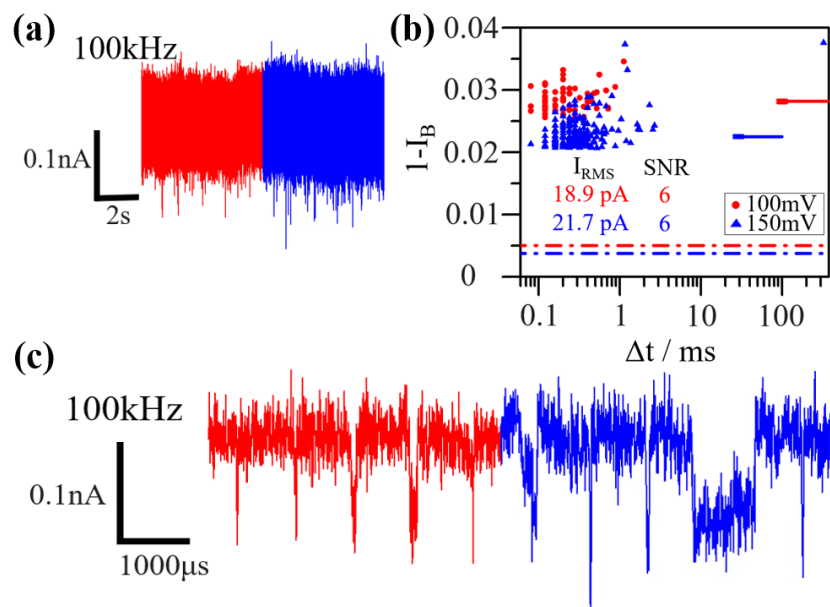
472 (e) Histograms of Δt of the segregated events based on two I_B populations, fitted by exponential

473 function. The translocation events (top panel) has a longer tail (decay constant $16.19 \mu\text{s}$) than the
474 collision events (lower panel, decay constant $8.45 \mu\text{s}$).



475
 476 Figure 5. Signal-to-noise ratio (SNR) comparison between the sapphire nanopore and the Si
 477 nanopore under 100 kHz filter frequency. (a) Scatter plot of the fractional blockade current I_B
 478 ($=i_b/i_o$) versus the dwelling time Δt of all the DNA events from the sapphire nanopore under
 479 different bias voltages from 50 mV to 150 mV. (b) The histograms of I_B of the sapphire nanopore.
 480 Two distinct peaks are observed and fitted by Gaussian function, corresponding to the
 481 translocation events (green bars) and the collision events (pink bars). (c) Scatter plot of the
 482 fractional blockade current I_B ($=i_b/i_o$) versus the dwelling time Δt of all the DNA events from the
 483 Si nanopore. (d) The histograms of I_B of the Si nanopore. Two distinct peaks are observed for 100
 484 mV and 150 mV biases and fitted by Gaussian function, corresponding to the translocation events

485 (green bars) and the collision events (pink bars). The signals at 50 mV bias displayed only one
486 obvious peak and not further segregated. (e-f) Scatter plot of $1-I_B (= \Delta I/i_0)$ versus the dwelling time
487 Δt of all the DNA translocation events (collision events removed) from the sapphire nanopore (e)
488 and Si nanopore (f). The dashed lines at the bottom are the values of I_{RMS}/i_0 , in which I_{RMS} is the
489 root-mean-square noise at open-pore state. The short solid lines are the peak values of $(1-I_B)$ in the
490 Gaussian distribution of the translocation events in (b) and (d). The error bars of the distribution
491 are added at the left edge of each short solid line. The SNR for each bias voltage is determined by
492 the ratio between the values of the DNA signals, indicated by the short solid lines, and their
493 corresponding noises, represented by the dashed lines of the same color. The values of SNR are
494 also given in the figures. DNA data are represented by black, red and blue dots in figure a, c, e,
495 and f for the collecting bias voltages as 50 mV, 100 mV, and 150 mV.



496
497 Figure 6. Analysis of Poly(A)₄₀ single-stranded (ss) DNA translocation events for the sapphire
498 nanopore under 100 kHz filter frequency. (a) The current trace of the DNA translocation events
499 under 100 kHz filter frequency. (b) Scatter plot of $1-I_B$ ($=\Delta I/i_0$) versus the dwelling time Δt of all
500 the DNA translocation events (collision events removed). The dashed lines at the bottom are the
501 values of I_{RMS}/i_0 , in which I_{RMS} is the root-mean-square noise at open-pore state. The short solid
502 lines are the peak values of $(1-I_B)$ in the Gaussian distribution of the translocation events. The
503 error bars of the distribution are added at the left edge of each short solid line. The SNR is given
504 by the ratio of the DNA signal (short solid lines) and the noise (dashed lines) for each tested
505 voltage. (c) Representative DNA events under 100 kHz filter frequency. Here the signals are
506 indicated by red and blue for bias voltages at 100 mV and 150 mV, respectively.

508 Supplementary information for

509 **Sapphire Nanopores for Low-Noise DNA Sensing**

510 Pengkun Xia^{1,2,3}, Jiawei Zuo^{1,2,3}, Pravin Paudel^{1,2}, Shinhyuk Choi^{1,2,3}, Xiahui Chen^{1,2,3}, Weisi
511 Song⁴, JongOne Im^{4,5}, Chao Wang^{1,2,3*}

512 ¹School of Electrical, Computer and Energy Engineering, Arizona State University, Tempe, AZ,
513 USA

514 ²Center for Photonic Innovation, Arizona State University, Tempe, AZ, USA

515 ³Biodesign Center for Molecular Design & Biomimetics, Arizona State University, Tempe, AZ,
516 USA

517 ⁴Biodesign Center for Single Molecule Biophysics, Arizona State University, Tempe, AZ, USA

518 ⁵Curent Address: INanoBio Inc., Scottsdale, AZ, USA

519 **Supplementary Note 1**

520 The power spectral density (PSD) of a solid-state nanopore can be described as ^{1,2,3}

$$521 \quad S = a_1 \frac{1}{f^\beta} + a_2 + a_3 f + a_4 f^2 \quad (1)$$

522 where f is frequency and $a_{1,2,3,4}$ are coefficients. S consists of the low-frequency flicker noise

523 $\frac{a_1}{f^\beta}$ ($1 < \beta < 2$)⁴, white thermal noise a_2 , dielectric noise ^{5,6} $a_3 f$, and capacitive noise ⁷ $a_4 f^2$. The

524 noise current at high frequencies (e.g. >10 kHz) is mainly contributed by the capacitive noise $a_4 f^2$

525 (Figure S1b). This noise is proportional to total input capacitance C_{total} with a PSD growing with

526 the square of frequency - $S_{amp} = (2\pi f C_{total} v_n)^2$, where v_n is the voltage noise density of the

527 input equivalent voltage thermal noise of the input amplifier ⁸. And in this high-frequency sensing

528 regime, $I_{RMS}(B) = \frac{2\pi}{\sqrt{3}} B^{3/2} C_{total} v_n \sqrt{S(B)}$ ^{7,9}.

529 The total input capacitance is estimated as $C_{total} = C_{sys} + C_{chip}$ ⁷, in which C_{sys} is the

530 capacitance from the measurement setup and C_{chip} is the nanopore chip capacitance. C_{sys} is

531 generally on the order of 10-20 pF and the optimized CMOS amplifier design can decrease it down

532 to less than 5pF ^{9,10}. Whereas, C_{chip} , which is composed of $C_m + C_s$, can be as large as hundreds

533 of pF or even a few nF. C_m is the membrane capacitance, which becomes negligible for small

534 membranes. However, C_s (stray capacitance), which is expressed as $C_{Si-B1} \parallel (C_{Si-B1} + C_{Si-B3})$

535 (Figure S1c) for first-order estimation, can be significant due to the significant amount of free

536 carriers in silicon (Si) substrate ⁹.

537 **Supplementary Note 2**

538 To estimate the relationship between the membrane and the mask dimensions, we assume L_2 is
539 parallel to L_1 and the etching follows an effective facet angle θ (Figure S5c), which is between the
540 exposed facets in the cavity and sapphire c-plane that can be empirically determined (Figure 2a).
541 It can be easily determined that $L_1 = L_2 + 2\sqrt{3}h / \tan \theta$, where h is the sapphire wafer thickness
542 and θ is an effective facet angle between.

543 Table S1. The calculation of the Si nanopore capacitance in Figure S1c.

Capacitance type	Material	Dielectric constant (ϵ)	Area (A)	Thickness (t)	(1) Calculation Method	Capacitance
C_{Si-B1}	Silicon nitride (C_1) and silicon oxide (C_2)	6.5 (ϵ_1) and 3.9 (ϵ_2)	$(2400\mu\text{m}/2)^2 \times \pi - (4.2 \times 4.7\mu\text{m})^2$ ^(#)	23nm (t_1) and 99nm (t_2)	$C_{Si-B1} = \frac{1}{1/C_1 + 1/C_2}$ $C_1 = \epsilon_1 \cdot \epsilon_0 \cdot A/t_1$ $C_2 = \epsilon_2 \cdot \epsilon_0 \cdot A/t_2$	1384pF
(1) $C_{Si-B2} + C_{Si-B3}$	Silicon oxide	3.9	$\approx (2400\mu\text{m}/2)^2 \times \pi$ ^(##)	(2) 2nm	$C_{Si-B2} + C_{Si-B3} = \epsilon \cdot \epsilon_0 \cdot \frac{A}{t}$	70106pF
C_m	Silicon nitride	6.5	$(4.2 \times 4.7\mu\text{m})^2$ ^(###)	23nm	$C_m = \epsilon \cdot \epsilon_0 \cdot \frac{A}{t}$	0.049pF
C_{total}					$C_{total} = C_m + C_{Si-B1} (C_{Si-B2} + C_{Si-B3})$	1360pF

544

545 C_{Si-B1} , $C_{Si-B2} + C_{Si-B3}$, C_m and C_{total} of the $4.2 \times 4.7\mu\text{m}$ (23 nm thick) membrane Si nanopore.^(#)

546 2400 μm is the real o-ring opening diameter, which was measured by stamping an o-ring pattern

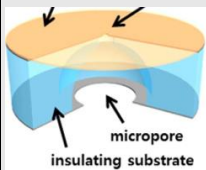
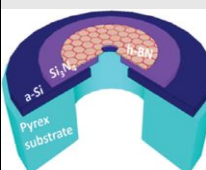
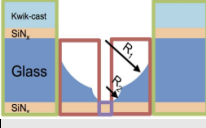
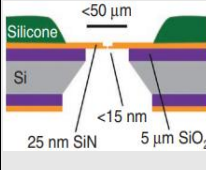
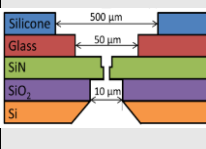
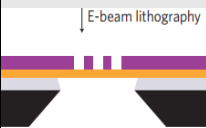
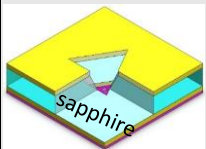
547 on a piece of paper using some ink. $4.2 \times 4.7\mu\text{m}$ is the square membrane side length.^(##) 2400 μm

548 is the o-ring opening diameter.^(###) $4.2 \times 4.7\mu\text{m}$ is the side length of the square membrane.⁽¹⁾ ϵ_0 is

549 the vacuum permittivity, 8.854 pF/m.⁽²⁾ For this chip, the bottom surface oxide layer (at the cavity

550 side) has the same thickness with the oxide in the back cavity (2 nm).

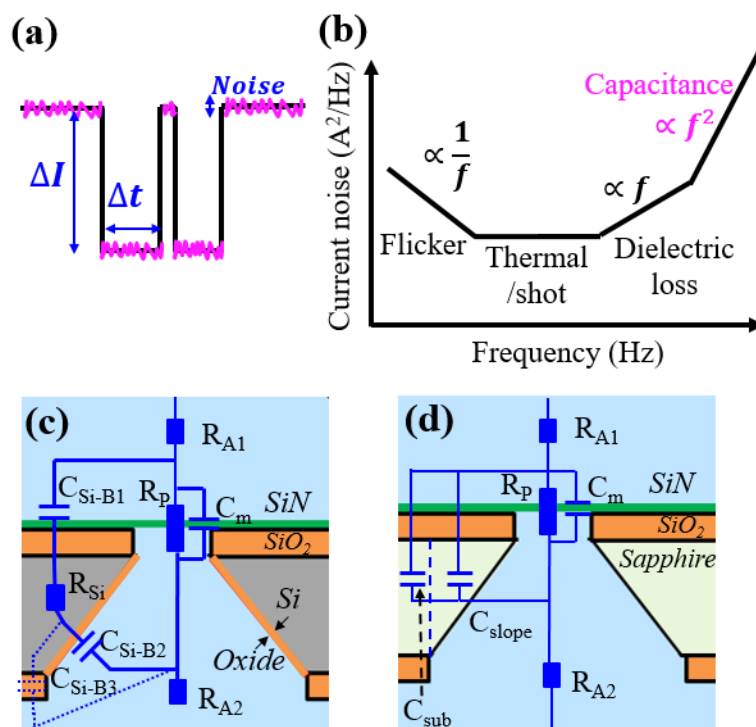
551 Table S2. Comparison of different methods to make low-noise solid-state nanopore chips.

Methods	Schematic	Substrate/ membrane	Membrane size/ thickness	Chip capacitance	RMS noise	Scalability and comments
HF etching glass & SiN membrane transfer		Glass/ Silicon nitride	$25\mu\text{m}^2$ / 20nm	70pF (measured)	12.58pA @4.5nA, 10kHz	Not scalable. ■ Manual transfer of SiN needed to keep the membrane dimension uniform.
HF etching glass & SiN membrane transfer		Glass/ Boron nitride	$0.0025\mu\text{m}^2$ / 2-3nm	5-10pF (measured)	4.3pA @0nA, 10kHz; 12.8pA @0nA, 100kHz	Not scalable. ■ Same as above. ■ Additional FIB drilling step is required to make the tiny window for suspending h-BN.
Two-step HF etching glass & Silicone painting		Glass/ Graphene	$0.071\mu\text{m}^2$ / 0.34nm	0.55- 1.25pF (calculated)	NA	Not scalable. ■ Uniformity and controllability are unknown for two- step etching. ■ Manual painting.
CMOS amplifier & EBL & Silicone painting		Silicon/ Silicon nitride	$0.25\mu\text{m}^2$ / 10-15nm	6pF (calculated)	7.2pA @10kHz; 12.9pA @100kHz (Bias info: NA)	Not scalable. ■ Manual painting. ■ Using EBL to pattern a small membrane is expensive.
Manual painting and bonding & EBL		Silicon/ Silicon nitride	100- $1600\mu\text{m}^2$ / sub 10nm	1.9-5.8pF (measured)	119- 149pA @1MHz (Bias info: NA)	Not scalable. ■ Manual painting and bonding. ■ EBL for small membrane. (expensive)
EBL		Silicon/ Silicon nitride	$0.0625\mu\text{m}^2$ / 6nm	NA	70-80pA @100kHz (Bias info: NA)	Not scalable. ■ EBL for small membrane. (expensive)
This work: Sapphire substrate		Sapphire/ Silicon nitride	$2002\mu\text{m}^2$ / 30nm	10pF (measured)/ 5.4pF (calculated)	■ 10kHz: 4.7pA @50mV ■ 100kHz: 17.7pA @50mV	Scalable. ■ Anisotropic etching of sapphire

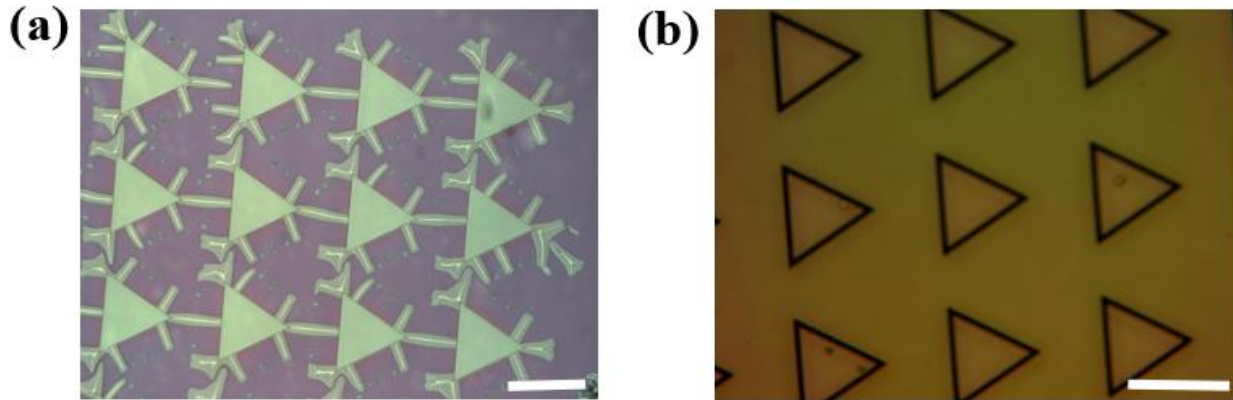
552 Table S3. The calculation of the sapphire nanopore capacitance in Figure S1d.

Capacitance type	Material	Dielectric constant (ϵ)	Area (A)	Thickness (t)	⁽¹⁾ Calculation Method	Capacitance
C_{sub}	Sapphire	9.3	$(2400\mu m/2)^2 \times \pi - (762\mu m/2)^2 \times \sqrt{3}$ ^(*)	$250\mu m$	$C_{sub} = \epsilon \cdot \epsilon_0 \cdot \frac{A}{t}$	1.4pF
C_{slope}	Sapphire	9.3	L ₂ edge to L ₁ edge ^(**)	$250\mu m$	$C_{slope} = \int_{L2\ edge}^{L1\ edge} \epsilon \cdot \epsilon_0 \cdot \frac{A(x)}{t(x)} dx$	0.2pF
C_m	Silicon nitride	6.5	$(5\mu m/2)^2 \times \sqrt{3}$ or $(68\mu m/2)^2 \times \sqrt{3}$ ^(***)	2nm or 30nm	$C_m = \epsilon \cdot \epsilon_0 \cdot \frac{A}{t}$	0.3pF or 3.8pF
C_{total}					$C_{total} = C_{sub} + C_{slope} + C_m$	1.9pF or 5.4pF

553
554 C_{sub} , C_{slope} , C_m and C_{total} of the $5\mu m$ wide (2 nm thick) or $68\mu m$ wide (30 nm thick) membrane
555 sapphire nanopore. ^(*) $2400\mu m$ is the o-ring opening diameter, and $762\mu m$ is L_1 . ^(**) Top-view
556 area between L_2 edge to L_1 edge. ^(***) $5\mu m$ is the side length L_2 of the triangular membrane. ⁽¹⁾ ϵ_0
557 is the vacuum permittivity, 8.854 pF/m.



558
 559 Figure S1. Motivation of designing low-noise solid-state nanopores in sapphire. (a) A schematic
 560 of typical DNA signals during the DNA translocating through a solid-state nanopore. ΔI is the
 561 blockade current amplitude, Δt is the dwelling time, and the pink ripples are the current noise. (b)
 562 The current noise contribution on the solid-state nanopores at different frequencies. One key noise
 563 contributor at high-frequency detection is the total input capacitance. (c) The equivalent circuit of
 564 a silicon-substrate solid-state nanopore, showing the parasitic capacitance (C_{Si-B1} , C_{Si-B2} and C_{Si-}
 565 $B3$) due to the existence of free carriers in the silicon substrate. (d) The equivalent circuit of a
 566 sapphire-substrate solid-state nanopore. No parasitic capacitance is observed due to the insulating
 567 property of the sapphire substrate. Instead, as a dielectric material, the capacitance from the thick
 568 sapphire itself (C_{sub} and C_{slope}) are very small.



569

570 Figure S2. Process development to achieve crack-free SiO₂ mask for reliable sapphire etching. (a)

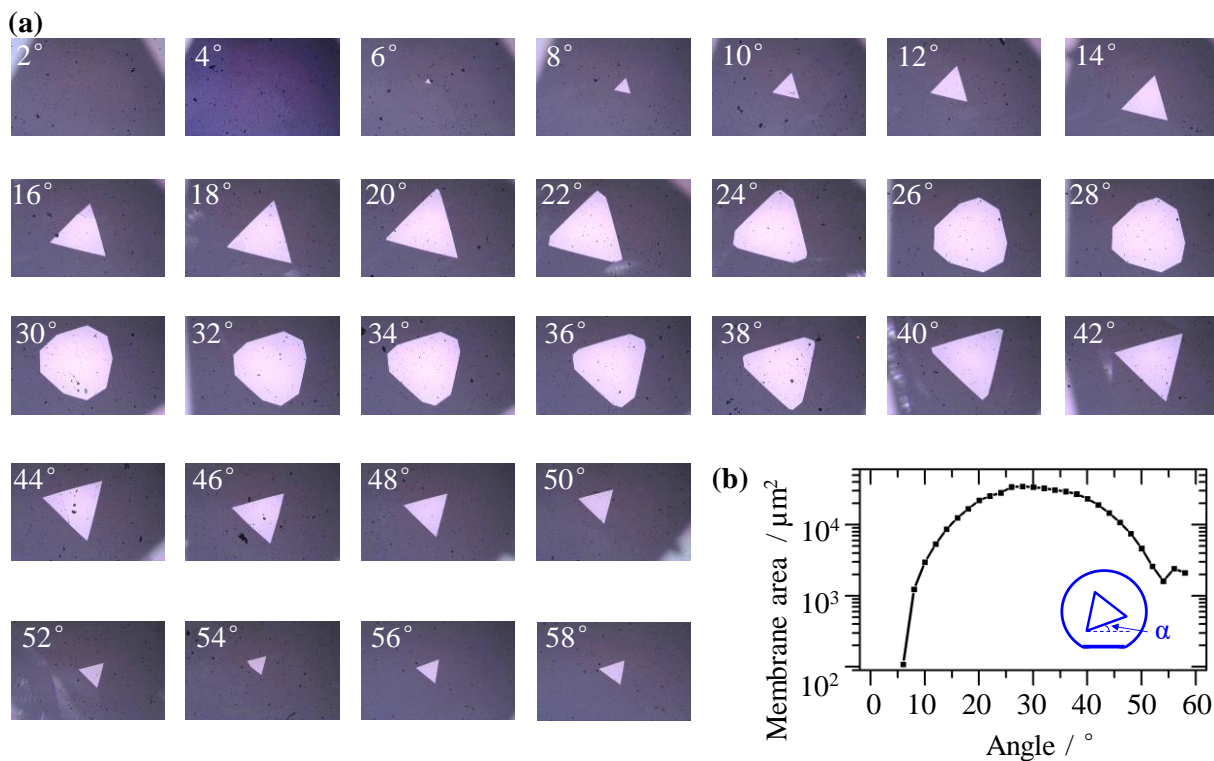
571 An optical image of a sapphire wafer with PECVD SiO₂ window patterned after 1-hour sapphire

572 etching @400°C hot-plate temperature. Severe undercut etching was observed. (b) An optical

573 image of the sapphire wafer with the same PECVD SiO₂ window after 2-hour sapphire etching

574 @450°C hot-plate temperature, with added RCA2 cleaning and thermal annealing prior to etching.

575 No undercut etching was observed.



576

577 Figure S3. Experimental analysis of the dependence of membrane shape and size (side length L_2)

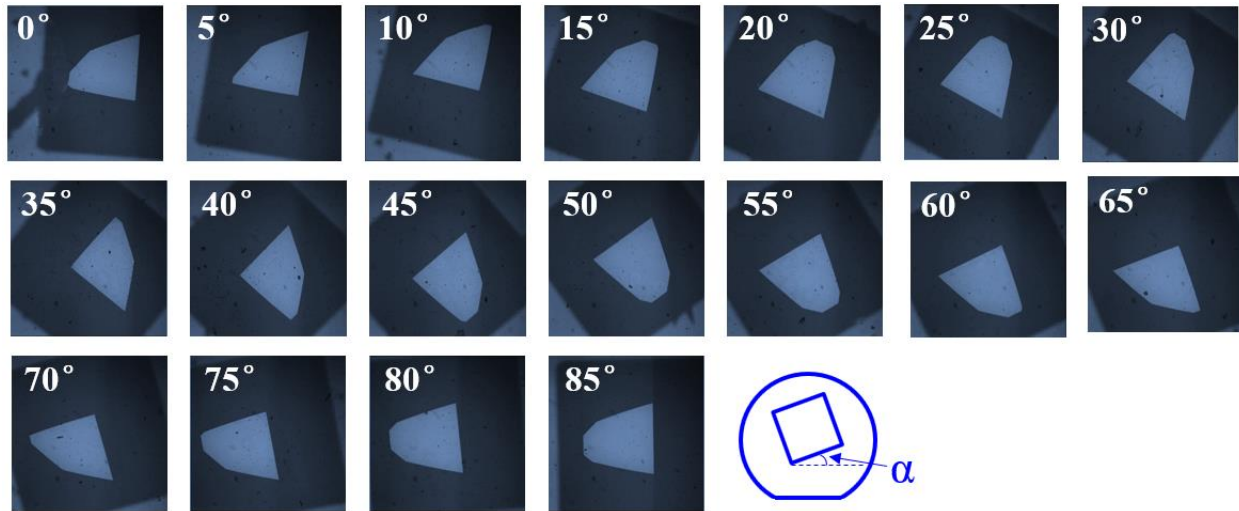
578 control on the alignment angle between the triangular-shaped etching windows (side length L_1)

579 and the A-plane sapphire flat. (a) Optical images of the membranes. The alignment angles (α ,

580 indicated in figure b) between the etching window and the A-plane sapphire flat is indicated on

581 the images. (b) The plot of the membrane area versus the alignment angle α . Here the etching

582 window size length L_2 was fixed as about $767 \mu\text{m}$. the sapphire was etched about $232 \mu\text{m}$.

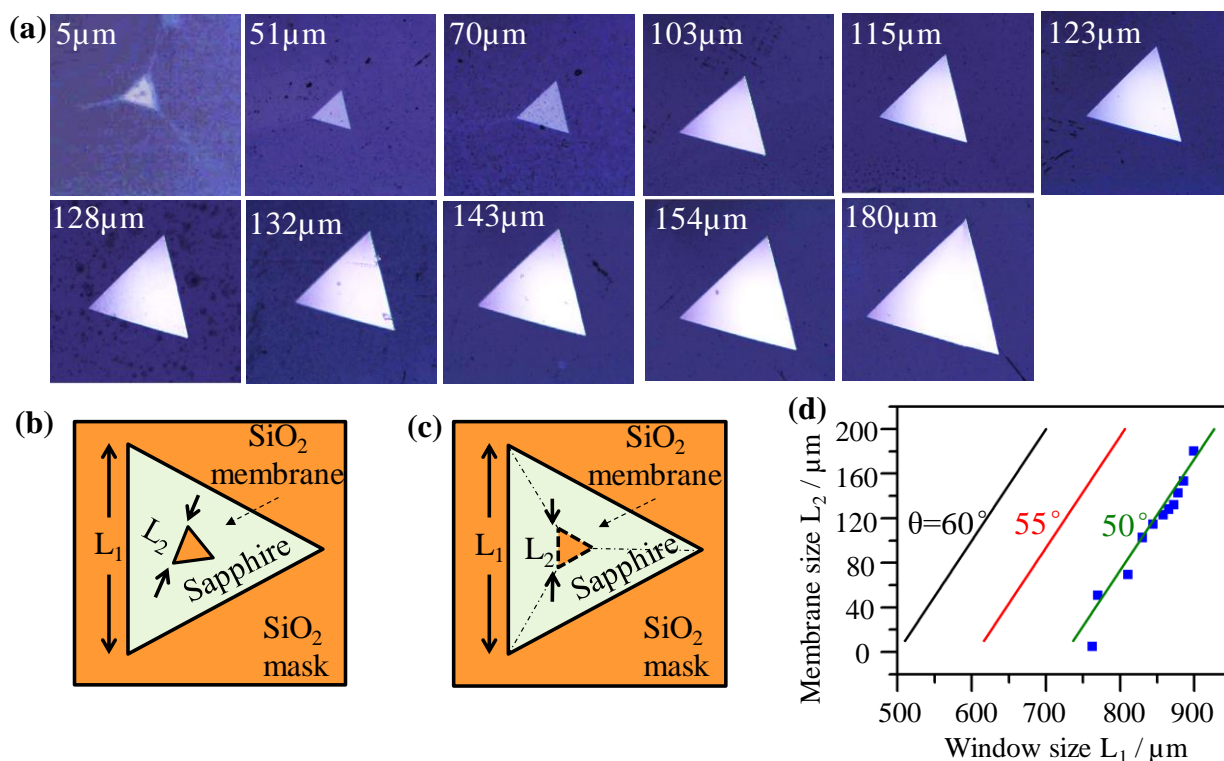


583

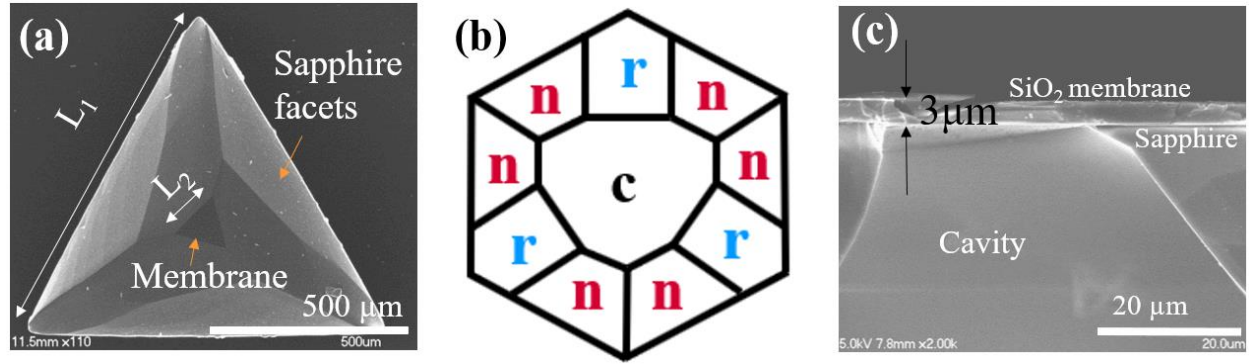
584 Figure S4. Optical images of the membranes formed on sapphire by square-shaped etching

585 windows (L_1) with different alignment angles. Here the window side length L_2 was fixed as 800

586 μm . The numbers on each image indicate the alignment angles α .



587
 588 Figure S5. Demonstration of tuning membrane dimension by engineering the etching mask
 589 dimensions. (a) Optical images of the membranes (side length L_1) with different etching window
 590 sizes (side length L_2). The numbers on the images indicate the value of L_2 . The magnification of
 591 the objective lens is 100x for the 5 μm triangle and 10x for others. (b) Top view of a real sapphire
 592 chip after the sapphire is etched through. There is an offset angle between L_1 and L_2 . (c) The
 593 membrane L_2 is assumed to be paralleled to L_1 to estimate the effective facet angle θ by applying
 594 the equation $L_1 = L_2 + 2\sqrt{3}h / \tan \theta$. (d) Plot of L_2 – L_1 relationship, fitted by a model assuming
 595 the sapphire etching follows an effective facet angle θ , which is the angle marked in Figure 2a.
 596 The fitting indicates the effective facet angle is around 50° while $\alpha=0^\circ$.



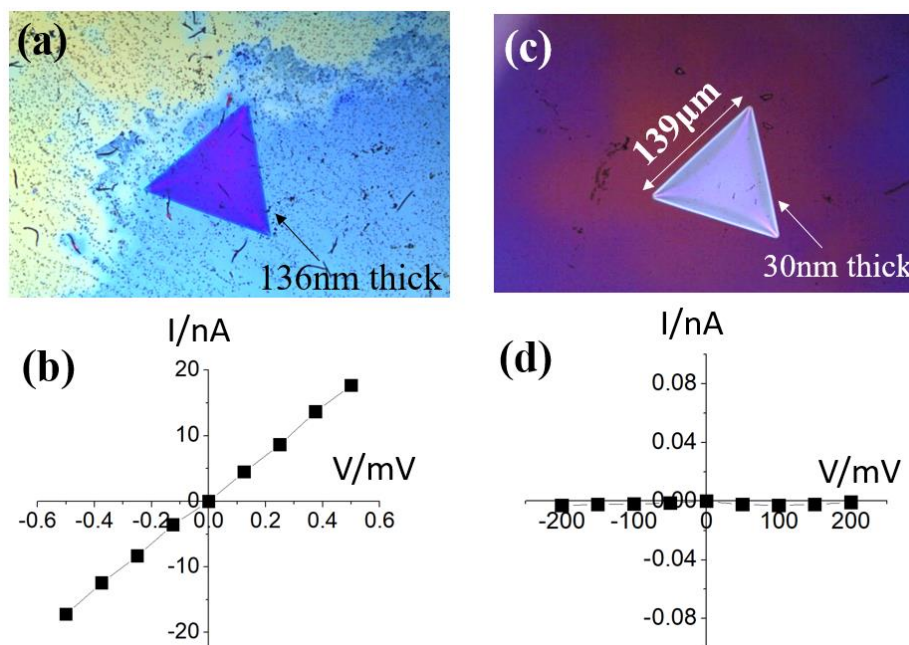
597

598 Figure S6. Facets of the sapphire in the cavity after sapphire etching. (a) The SEM image of the

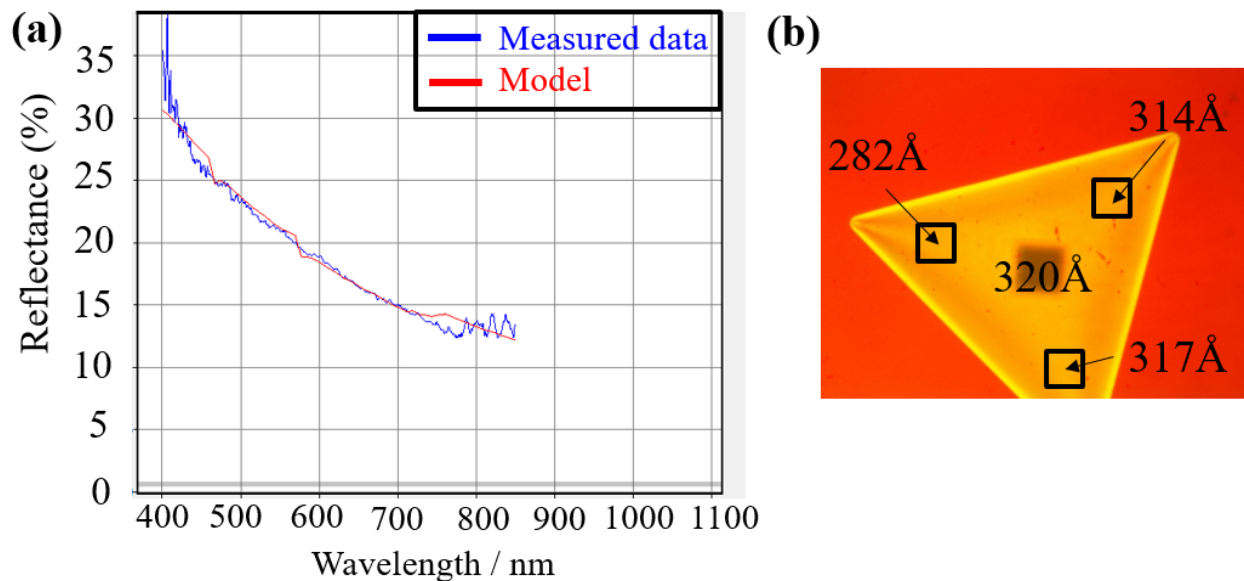
599 top view of the sapphire cavity. (b) The three-fold symmetric n-r-n plane system, which caused

600 the three-fold symmetric etching facets of sapphire. (c) The SEM image of the cross section of

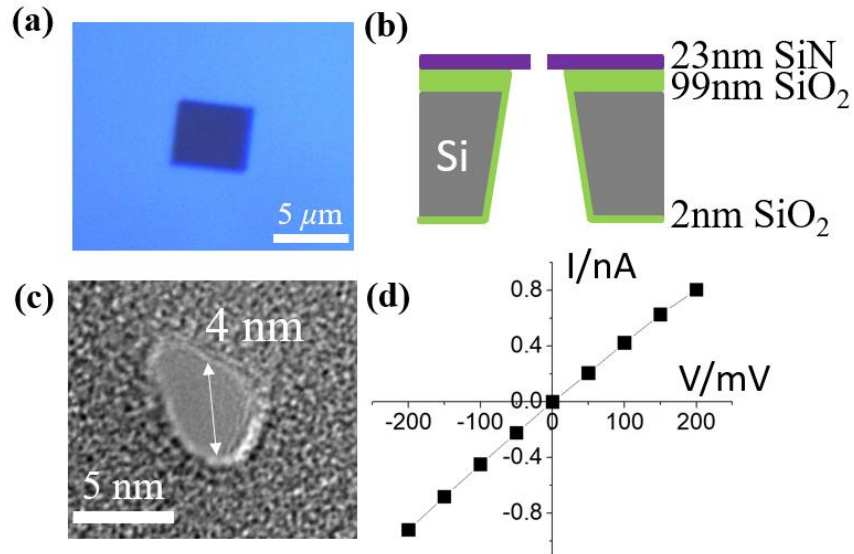
601 the sapphire cavity.



602
603 Figure S7. Comparison of thinning down the SiN membrane by reactive-ion etching (RIE) or
604 phosphoric acid wet etching. (a) Optical image of a SiN membrane after RIE dry etching (thickness
605 after etching: 136 nm). RIE recipe: PlasmaTherm 790 RIE Fluorine (tool), 30 W bias, 100 mTorr,
606 CF_4 50 sccm, O_2 2 sccm, etching rate: 18 nm/min (b) Optical image of a SiN membrane after hot
607 phosphoric wet etching (thickness after etching: 30 nm). (c) current-voltage (IV) characteristic of
608 the membrane in figure a in 1M KCl solution. (d) IV characteristic of the membrane in figure b in
609 1M KCl solution.

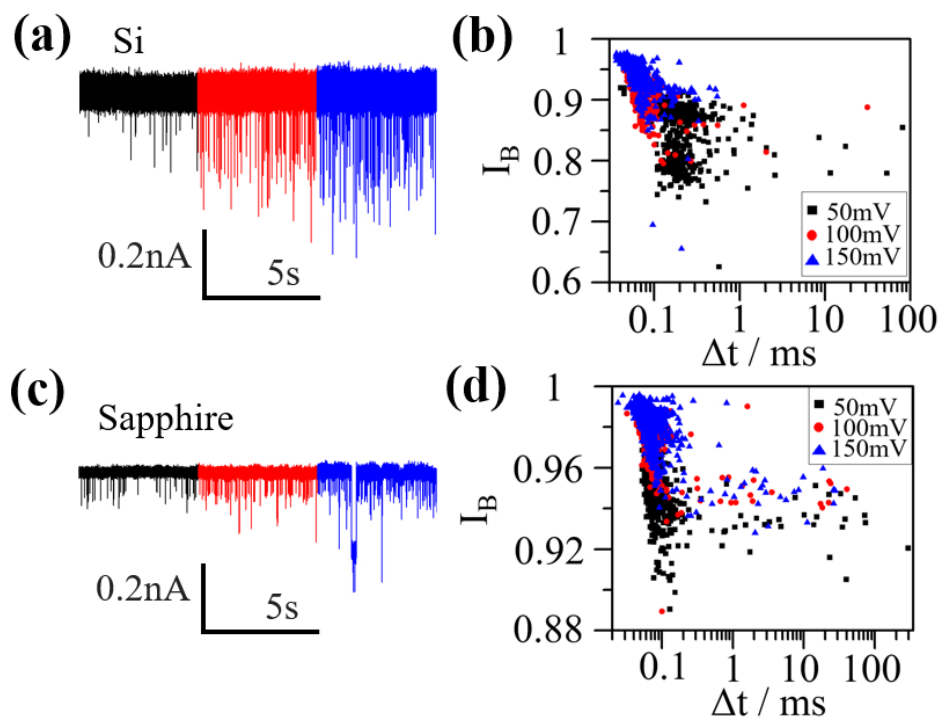


610
611 Figure S8. The thickness characterization of the membrane thickness using Filmetrics F40. (a) The
612 fitting curve (red) of the measured reflectance spectrum of the SiN membrane (blue). (b) The
613 uniformity characterization of the membrane thickness. The thickness variation of the left corner
614 may come from the bending of the membrane, since F40 measurement is based on the reflectance
615 of light.

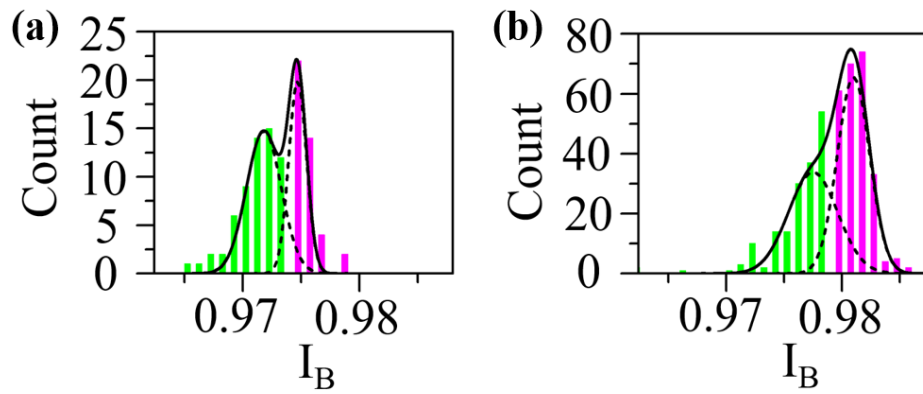


616

617 Figure S9. The small-membrane Si nanopore chip for comparison. (a) The optical image of the
618 SiN membrane (4.2 μm by 4.7 μm). (b) The schematic of the structure of this nanopore chip. (c)
619 The nanopore drilled by TEM on the SiN membrane. (d) The IV curve tested by 100 mM KCl
620 solution, showing good linearity.



621
622 Figure S10. Representative 1kbp dsDNA translocation events for the sapphire nanopore and the Si
623 nanopore under 10kHz filter bandwidth. (a) The current trace of the DNA translocation events of
624 the Si nanopore under different voltages (black: 50 mV, red: 100 mV, blue: 150 mV). (b) Scatter
625 plot of the fractional blockade current $I_B (=i_b/i_0)$ versus the dwelling time Δt of all the DNA events
626 from the Si nanopore under different voltages (black: 50 mV, red: 100 mV, blue: 150 mV). (c) The
627 current trace of the DNA translocation events of the sapphire nanopore under different voltages
628 (black: 50 mV, red: 100 mV, blue: 150 mV). (d) Scatter plot of the fractional blockade current I_B
629 ($=i_b/i_0$) versus the dwelling time Δt of all the DNA events from the sapphire nanopore under
630 different voltages (black: 50 mV, red: 100 mV, blue: 150 mV).



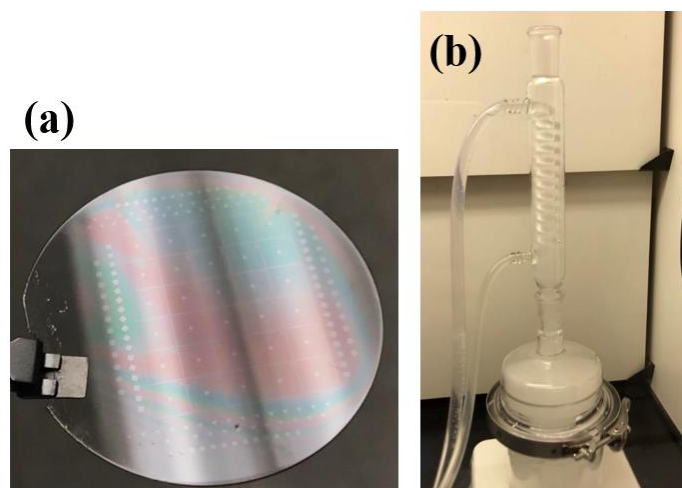
631

632 Figure S11. The histograms of I_B from the analysis of Poly(A)₄₀ single-stranded (ss) DNA by the

633 sapphire nanopore under 100 mV (a) and 150 mV (b). Two distinct peaks are observed and fitted

634 by Gaussian function, corresponding to the translocation events (green bars) and the collision

635 events (pink bars).



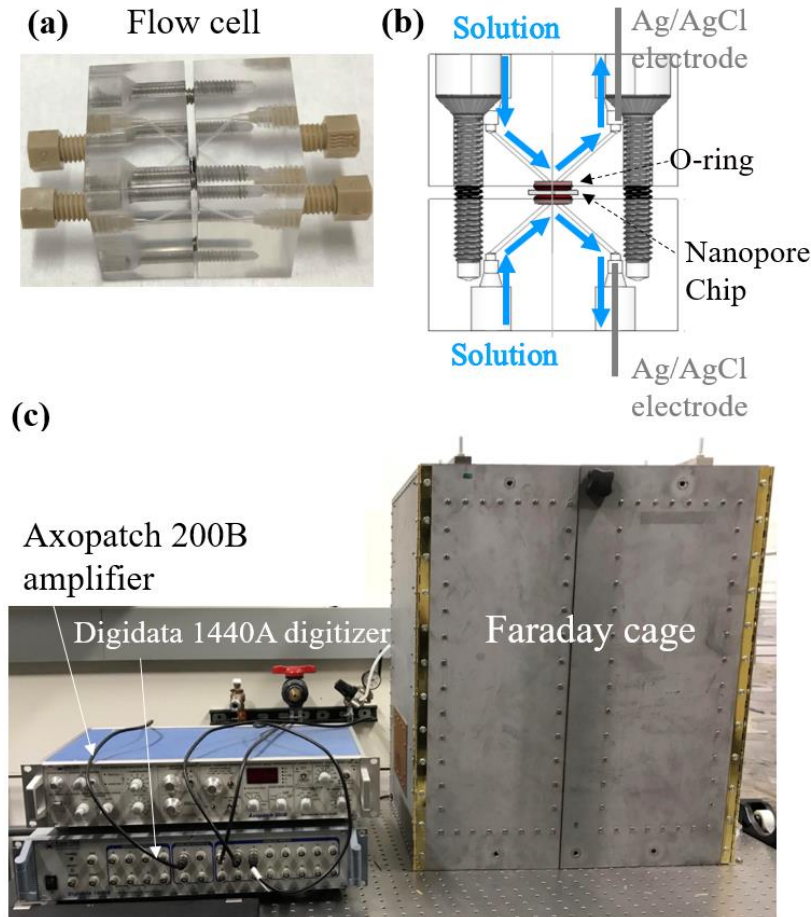
636

637 Figure S12. Optical graphs of: (a) A sapphire wafer with SiO₂ mask patterned right before the

638 sapphire etching. (b) The glassware setup used for sapphire etching: The glass vessel and its lid

639 are clamped together by a stainless-steel clamp. On the top, a water condenser is used to condense

640 and recirculate the evaporated acid. The setup is put on a hot plate.



641

642 Figure S13. The experimental setup for the noise characterization and DNA sensing of the

643 nanopore chip. (a) A photo of the flow cell used for providing electrolyte ambient for the nanopore

644 chip. It is composed of two acrylic pieces drilled with fluidic channels. The two pieces are mounted

645 together by four screws. (b) A schematic of the flow cell showing the injection of the electrolyte

646 solution (blue path) and the mounted nanopore chip. (c) The Faraday cage used to contain the flow

647 cell to isolate the environment noise and the Axopatch 200B amplifier with the Digidata 1440A

648 digitizer.

649 **Supplementary References**

- 650 1. Tabard-Cossa V, Trivedi D, Wiggin M, Jetha NN, Marziali A. Noise analysis and
651 reduction in solid-state nanopores. *Nanotechnology* 2007, **18**(30): 305505.
- 652 2. Dimitrov V, Mirsaidov U, Wang D, Sorsch T, Mansfield W, Miner J, *et al.* Nanopores in
653 solid-state membranes engineered for single molecule detection. *Nanotechnology* 2010,
654 **21**(6): 065502.
- 655 3. Wen C, Zeng S, Arstila K, Sajavaara T, Zhu Y, Zhang Z, *et al.* Generalized noise study
656 of solid-state nanopores at low frequencies. *ACS sensors* 2017, **2**(2): 300-307.
- 657 4. Siwy Z, Fuliński A. Origin of $1/f$ noise in membrane channel currents. *Physical Review*
658 *Letters* 2002, **89**(15): 158101.
- 659 5. Uram JD, Ke K, Mayer M. Noise and bandwidth of current recordings from
660 submicrometer pores and nanopores. *Acs Nano* 2008, **2**(5): 857-872.
- 661 6. Levis RA, Rae JL. The use of quartz patch pipettes for low noise single channel
662 recording. *Biophysical journal* 1993, **65**(4): 1666-1677.
- 663 7. Balan A, Machielse B, Niedzwiecki D, Lin J, Ong P, Engelke R, *et al.* Improving signal-
664 to-noise performance for DNA translocation in solid-state nanopores at MHz bandwidths.
665 *Nano letters* 2014, **14**(12): 7215-7220.
- 666 8. Ferrari G, Gozzini F, Molari A, Sampietro M. Transimpedance amplifier for high
667 sensitivity current measurements on nanodevices. *IEEE Journal of Solid-State Circuits*
668 2009, **44**(5): 1609-1616.
- 669 9. Rosenstein JK, Wanunu M, Merchant CA, Drndic M, Shepard KL. Integrated nanopore
670 sensing platform with sub-microsecond temporal resolution. *Nature methods* 2012, **9**(5):
671 487.

- 672 10. Shekar S, Niedzwiecki DJ, Chien C-C, Ong P, Fleischer DA, Lin J, *et al.* Measurement of
673 DNA translocation dynamics in a solid-state nanopore at 100 ns temporal resolution.
674 *Nano letters* 2016, **16**(7): 4483-4489.